International Journal of Mechanical Sciences 238 (2023) 107861

Contents lists available at ScienceDirect

International Journal of Mechanical Sciences

journal homepage: www.elsevier.com/locate/ijmecsci

Programming curvatures by unfolding of the triangular Resch pattern

Ying Yu [a], Yan Chen [b], Glaucio Paulino [c,d,e,*]

[a] *Department of Civil Engineering, Shantou University, Shantou 515063, China*
[b] *School of Mechanical Engineering, Tianjin University, Tianjin 300072, China*
[c] *Department of Civil and Environmental Engineering, Princeton University, Princeton, NJ 08544, USA*
[d] *Princeton Institute for the Science and Technology of Materials, Princeton University, Princeton, NJ 08544, USA*
[e] *Department of Mechanical and Aerospace Engineering, Princeton University, Princeton, NJ 08544, USA*

ARTICLE INFO

Keywords:
Programmable curvatures
Resch pattern
Finite particle method
Unfolding
Constraints

ABSTRACT

The multi-degree of freedom Resch pattern forms most of its surfaces by tuning the folding angles of its creases. In this research, we program the triangular Resch pattern to naturally achieve surfaces with various curvatures by predefining the neutral angle and stiffness of the creases for the whole pattern. We simulate the free unfolding of tessellations by combining a "bar-and-hinge" model with an explicit meshless method, namely, the finite particle method. The effects of the damping factor, crease stiffness, and neutral angle on the unfolding process are investigated. The neutral angle of the creases plays a critical role in determining the final stable shape of the pattern. Then, we break the natural symmetry of the tessellations by changing the neutral angle and applying specific constraints to active creases to create stable unfolding surfaces with various curvatures. This study provides a foundation for the development of programmed curvatures of metamaterials that can be folded into origami patterns with multiple degrees of freedom.

1. Introduction

Deforming flat sheets into curved geometries is an ancient mathematical problem. To create arbitrarily complex three-dimensional (3D) structures from two-dimensional (2D) sheets, it is necessary to transform flat sheets using a method such as Gauss's Theorema Egregium or Chebyshev's solution for modelling curved cloth [1]. Flat sheets can be easily bent and rolled into simple curved shapes, such as arches and cylinders. However, to achieve complex shapes, such as spherical and hyperbolic geometries, it is necessary to distort and shear flat sheets. For example, to create a hyperbolic surface, different materials, such as flat metal sheets and fibre-reinforced composite laminates must be plastically stretched and sheared [2–5].

The main disadvantage of achieving complex 3D surface geometries through the deformation of 2D sheets is that this method damages stiff materials. Fortunately, origami provides an alternative method for obtaining complex 3D surface geometries from rigid 2D materials with various surfaces [6,7]. The rich mathematical underpinning and tunable mechanical properties of origami, in combination with a variety of advancing technologies, have led to exciting applications in science and engineering [8–11]. For example, the principles of origami have been used to guide the design of tunable bandgap structures [12,13], solar cells and antennas [8,14,15], self-folding robots [14,16,17], and metamaterials [18–22].

The use of origami for making 3D curved surfaces has attracted considerable attention among researchers [6,23]. Many advances have been achieved in the development of methods for fitting origami patterns to 3D surfaces [24,25]. Schenk and Guest [26] identified the saddle and twist deformation modes of the nonrigid Miura pattern and found that this origami tessellation was suitable for complex surface fitting. Gattas et al. [27] explored five rigidly foldable "first-level derivatives" of the Miura pattern, which could achieve an overall single or double curvature. Dudte et al. [28] developed a generalized optimization algorithm to solve the inverse problem of fitting an intrinsically curved surface with the Miura pattern. Although the exact curvature of intrinsically curved surfaces could not be guaranteed with this algorithm, various 3D surfaces could be approximated using flat, foldable, and rigid origami tessellations.

In addition to the Miura pattern, several other origami tessellations have been used for fitting curved surfaces [29,30]. Resch and Christiansen [31] attempted to fold the Resch pattern into the shape of an egg, namely, the Vegreville Easter egg. To do so, they had to cut some of the middle tucks of the Resch pattern in such a manner that it became a Kagome lattice capable of fitting surfaces [32]. Tachi [33] demonstrated

---

[*] Corresponding author.
E-mail addresses: yuying@stu.edu.cn (Y. Yu), yan_chen@tju.edu.cn (Y. Chen), gpaulino@princeton.edu (G. Paulino).

https://doi.org/10.1016/j.ijmecsci.2022.107861
Received 7 June 2022; Received in revised form 18 October 2022; Accepted 18 October 2022

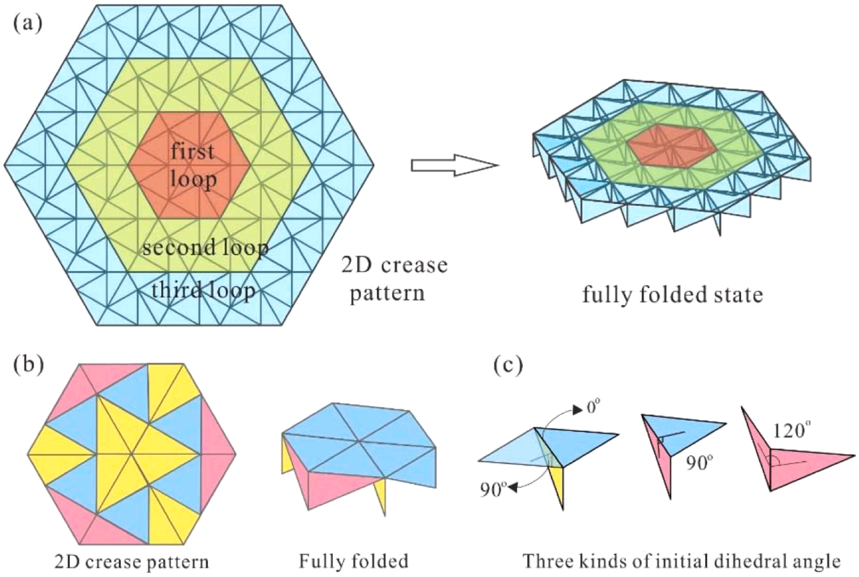

Fig. 1. Triangular Resch pattern. (a) The 2D crease pattern with three loops and the fully folded state of the pattern. (b) The 2D crease pattern and the fully folded state of one unit of the triangular Resch pattern. (c) Three types of creases with different folding angles of one unit, namely, 0°, 90°, and 120° The panel color in (c) corresponds to the panel color in (b).

that the smooth rigid folding of (triangulated) periodic tessellations into domed shapes was obstructed by excessively large tessellated sheets; under such conditions, only cylindrical surfaces could be obtained from periodic tessellations. Nassar et al. [34] reached a similar conclusion.

The aforementioned studies mainly focused on folding flat sheets to produce specific shapes and geometric patterns. However, since the unfolding of an origami tessellation from a fully folded state is driven by the energy stored in its creases, it can achieve a natural equilibrium configuration. Rich 3D geometries can be achieved by unfolding origami tessellations with multiple degrees of freedom (DOFs). Different crease stiffnesses and unfolding sequences lead to distinct curvatures in the final configuration. Thus, origami tessellations can be unfolded to program a surface. In this study, we explored how to tune a suitable surface curvature by unfolding the Resch pattern to an intermediate level of deployment between the fully folded state and the 2D-sheet state.

The numerical analysis of origami patterns is mainly conducted through reduced models, which focus on the approximate global behavior of a pattern rather than high-resolution study of local deformations [35–37]. In the “bar-and-hinge” model proposed by Schenk and Guest [26], an origami pattern is triangulated to form a truss framework with constrained rotational hinges. Improved versions of this model can be used to analyze the bending of the Miura pattern [38], optimize the topology of origami structures [39] and geometry description of a cylindrical origami structures with waterbomb pattern [40]. Most models used for the numerical analysis of origami patterns involve linear analysis of small deformations. However, Barbieri et al. [41] used large deformations and large rotations within a first-order shear plate theory to simulate folding as sharp discontinuities in the Euler rotations of nonlinear plates. Liu and Paulino [42,43] developed a general nonlinear formulation that considered material and geometric nonlinearities for the structural analysis of origami structures associated with arbitrary “bar-and-hinge” models.

Although current numerical models for the analysis of origami patterns can analyze rigid and nonrigid origami motions, most of them use a static or quasi-static folding process for analysis [44–47]. Some researchers have studied the dynamic folding behavior of origami structures. Fang et al. [48] performed an experimental and analytical study on the dynamic folding of stacked Miura-Ori structure with intrinsic bi-stability. Sadeghi and Li [49] examined a rapid and reversible origami dynamic folding method by exploiting a combination of resonance excitation, asymmetric multi-stability, and active control. Wu et al. [50] studied the transient dynamics of a Miura-Origami tube during free deployment. So, it is worthwhile to investigate the dynamic unfolding of origami tessellations to reach their natural unfolded configurations; this process is driven by the energy stored in the creases. Yu et al. [51,52] verified that an explicit meshless method called the finite particle method (FPM) can simultaneously calculate large rigid body motions and large geometrical changes of deployable structures based on the straight-rod hinge and angulated-rod hinge. Furthermore, Yu et al. [53] showed the possibility of combining “bar-and-hinge” model and the FPM for dynamic analysis of origami. Therefore, in this study, the “bar-and-particle” model was proposed by combining the “bar-and-hinge” model with the FPM to simulate the dynamic unfolding of the triangular Resch pattern and program this pattern to naturally achieve surfaces with various curvatures.

The remainder of this paper is structured as follows. The parameters of the Resch pattern are described in Section 2. Section 3 describes the modelling of the Resch tessellation with the proposed method for capturing the dynamics of unfolding. Section 4 details how the curvature of the Resch pattern’s intermediate unfolded states is varied by locally tuning the mechanical properties of the creases (i.e., the neutral angles), and Section 5 presents the conclusions of this study.

2. Kinematics and parameters of the triangular Resch pattern

The triangular Resch pattern comprises multiple equal-sized triangular units. Fig. 1(a) shows the 2D crease pattern with three loops and the fully folded state of the triangular Resch pattern [54–56]. The first loop is regarded as one unit of the triangular Resch pattern (Fig. 1b). Magliozzi et al. [57] reported that arbitrarily controlling all the DOFs of a multiple-DOF origami pattern is impossible. In the present study, starting from the fully folded configuration, the Resch pattern is unfolded using only the elastic energy stored in the creases and without using any additional bars or constraints. Thus, the structure is unfolded naturally, and no blocks occur during the unfolding process.

As displayed in Fig. 1(c), one fully folded unit contains three types of creases with different folding angles, namely, 0°, 90°, and 120° Because the unfolding of the triangular Resch pattern is triggered by the elastic energy stored in the creases, this pattern has maximum energy in the fully folded state. The crease with a dihedral angle of 0° stores

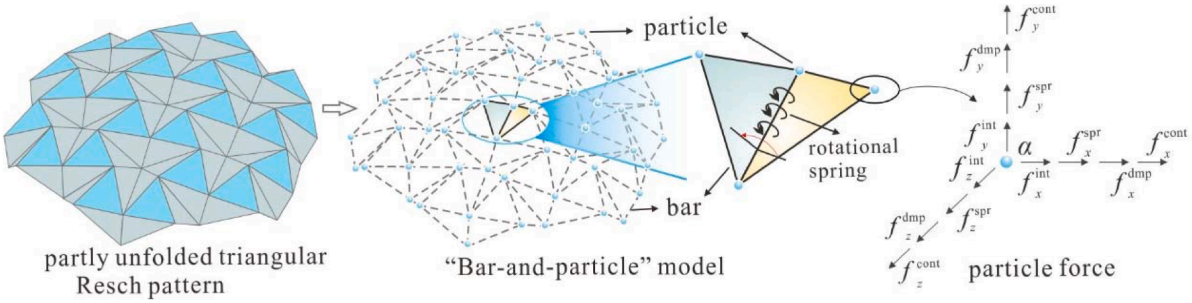

Fig. 2. "Bar-and-particle" model of the triangular Resch pattern. Blue particles are placed on the vertices of the origami panels, and bars are placed along straight dashed lines. Rotational springs are placed along the bars between two adjacent panels. Each particle has three translational DOFs and is in the dynamic equilibrium state under internal force, external force, damping force and contact force.

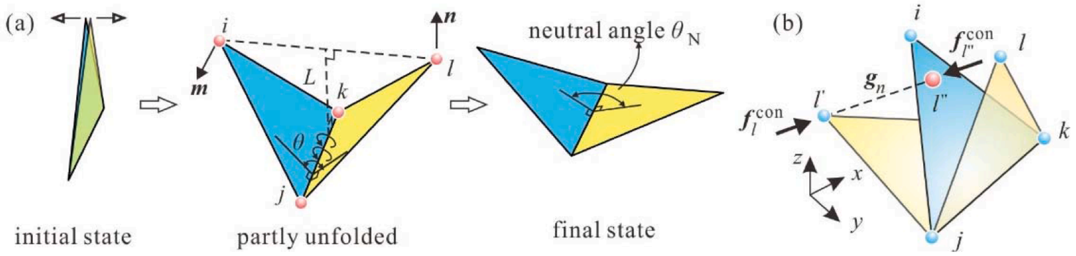

Fig. 3. Unfolding and contact models of a simple fold. (a) Unfolding process of the simple fold by the energy released stored in the origami crease. The dihedral angle reaches the neutral angle at the final state. (b) shows the contact model of the penetration between particles *i* and *l* at the initial state. A virtual particle l'' is defined to build a point-to-point collision.

considerably more energy than do the creases with the other folding angles when the pattern is fully folded.

3. Fundamentals of the FPM for origami unfolding simulation

In this section, the "bar-and-hinge" model is first combined with the FPM as the "bar-and-particle" model for conducting origami modelling in the FPM and simulating the dynamic unfolding of the triangular Resch pattern. Second, the equilibrium equation of an arbitrary particle in the origami system is constructed and solved through explicit time integration. Third, each component of the particle force (axial deformation of the creases, rotational deformation of the hinges, and damping) and the contact between adjacent particles are derived.

The FPM is tailored for nonlinear dynamic analysis. As per Newton's second law, each particle is in dynamic equilibrium during the unfolding of origami tessellations. The motion equation for each particle is explicit and can be easily solved without iteration. Through the use of a fictitious motion, the rigid body motion and pure deformation can be separated from the particle displacement. Therefore, geometric nonlinearity is addressed naturally by this method [52,58]. Researchers have used the FPM to study the dynamic unfolding process of origami tessellations, and their results have revealed the global dynamic response and free unfolding trajectories of origami structures [59,60].

3.1. Bar-and-particle model and equation of motion of a particle

The triangular Resch pattern is modelled as a triangulated truss with particles, bars, and constrained rotational springs, as indicated in Fig. 2. Particles are placed on the vertices of the origami panels, and bars are placed along straight fold lines. Rotational springs are placed along the bars between two adjacent panels to model the folding of creases. The structural mass is concentrated at the particles, whereas the bars has no mass. Each particle has three translational DOFs. According to Newton's second law, the motion equation for an arbitrary particle α is as follows:

$$m_\alpha \ddot{\mathbf{d}}_\alpha = \mathbf{f}_\alpha^{\mathrm{int}} + \mathbf{f}_\alpha^{\mathrm{spr}} + \mathbf{f}_s^{\mathrm{dmp}} + \mathbf{f}_\alpha^{\mathrm{cont}} \tag{1}$$

where m_α is the mass of particle α, $\ddot{\mathbf{d}}_\alpha$ is the acceleration vector of particle α, and $\mathbf{f}_\alpha^{\mathrm{int}}$ is the particle internal force vector generated by the deformation of bars connected to the particle. The derivation of $\mathbf{f}_\alpha^{\mathrm{int}}$ is detailed in Appendix A. The parameter $\mathbf{f}_\alpha^{\mathrm{spr}}$ represents the particle force vector generated by the deformation of the rotational springs located along all the creases connected to α. The parameter $\mathbf{f}_\alpha^{\mathrm{dmp}}$ represents the damping force vector of particle α, and this vector is expressed as follows: $\mathbf{f}_\alpha^{\mathrm{dmp}} = -\mu M_\alpha \dot{\mathbf{d}}_\alpha$. In FPM analysis based on an explicit formulation, artificial damping must be used to curb structural vibration [38,61,62]. The damping factor is denoted by μ, and the determination of μ is similar to the dynamic relaxation method [63,64]. The parameter $\mathbf{f}_\alpha^{\mathrm{cont}}$ denotes the vector of the contact force applied to particle α when penetration occurs between α and other particles or panels.

Explicit time integration with a central difference scheme is adopted to solve Eq. (1) [51,52]. Because all the particle forces, namely, $\mathbf{f}_\alpha^{\mathrm{int}}$, $\mathbf{f}_\alpha^{\mathrm{spr}}$, $\mathbf{f}_\alpha^{\mathrm{dmp}}$, and $\mathbf{f}_\alpha^{\mathrm{cont}}$, can be explicitly expressed, the displacement $\boldsymbol{d}_{n+1}$ at step $(n+1)$ can be determined using the following equation:

$$\begin{aligned}\mathbf{d}_{n+1} = {} & \left(\frac{2}{2+\mu\Delta t}\right)\frac{\Delta t^2}{m_\alpha}\left(\mathbf{f}_\alpha^{\mathrm{int}} + \mathbf{f}_\alpha^{\mathrm{spr}} + \mathbf{f}_\alpha^{\mathrm{dmp}} + \mathbf{f}_\alpha^{\mathrm{cont}}\right) + \left(\frac{4}{2+\mu\Delta t}\right)\mathbf{d}_n \\ & - \left(\frac{2-\mu\Delta t}{2+\mu\Delta t}\right)\mathbf{d}_{n-1}\end{aligned} \tag{2}$$

where d_n and d_{n-1} are the displacements vectors in steps n and $n-1$, respectively, and Δt is the time increment between steps n and $n+1$.

3.2. Particle force generated by a rotational spring

This section describes how to convert the energy released by an origami crease into a particle force that unfolds an origami pattern. Consider an example of a simple fold with two adjacent triangular panels (*ijk* and *lkj*) and one crease (*kj*), as shown in Fig. 3(a). A rotational spring is placed along the bar between *ijk* and *lkj* to represent a folding crease. The spring rotation can be determined from the variation in the dihedral

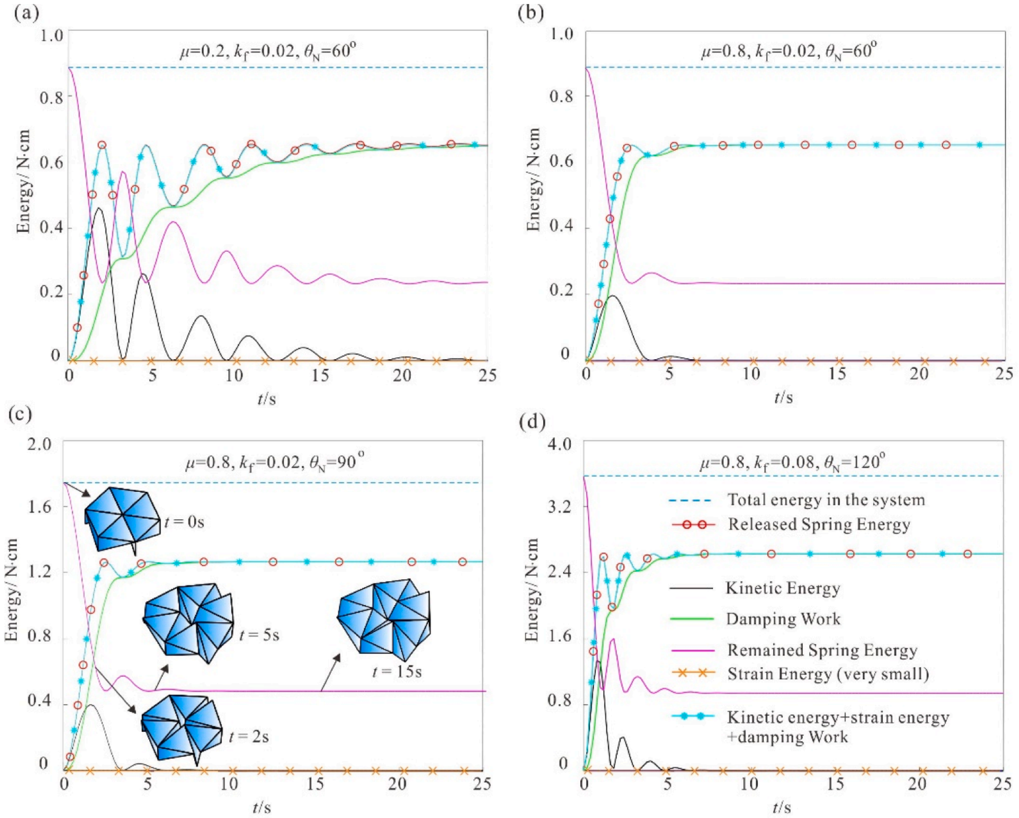

Fig. 4. Energy conservation study for a one-loop triangular Resch pattern during the unfolding process. (a) $\mu = 0.2$, $k_f = 0.02$ N/rad, and $\theta_N = 60°$; (b) $\mu = 0.8$, $k_f = 0.02$ N/rad, and $\theta_N = 60°$; (c) $\mu = 0.8$, $k_f = 0.02$ N/rad, $\theta_N = 90°$; and (d) $\mu = 0.8$, $k_f = 0.08$ N/rad, and $\theta_N = 120°$ The meanings of different line styles are indicated in (d). (c) also shows the unfolding process of a unit of the triangular Resch pattern.

angle θ between the two panels.

Because we are examining the unfolding process of origami patterns, the initial configuration for the simple fold is considered to be the fully folded configuration fixed by some constraints. The energy stored in the simple fold is maximum in the initial state. After the constraints are removed, driven by the energy stored in the crease *kj*, the simple fold begins to unfold until the dihedral angle between the two panels reaches the neutral angle θ_N of the crease. When the simple fold is at the neutral angle, the fold is in a stationary state, and the crease can release no additional energy. Thus, the stored energy $U_{\mathrm{spr}}^{\mathrm{int}}$ of the rotational spring is directly related to the dihedral angle θ. The total stored energy in a rotational spring element is a function of the dihedral angle and is expressed as follows:

$$U_{\mathrm{spr}}^{\mathrm{int}} = \mathrm{H}(\theta) \tag{3}$$

The resistance moment *M* can be defined as follows:

$$M = \frac{\partial \mathrm{H}(\theta)}{\partial \theta} \tag{4}$$

The particle internal force vector associated with a rotational spring element is determined as follows:

$$\mathbf{f} = \begin{bmatrix} f_i & f_l & f_j & f_k \end{bmatrix}^{\mathrm{T}} = \frac{\partial H}{\partial \theta}\frac{\partial \theta}{\partial \mathbf{x}} = M\frac{\partial \theta}{\partial \mathbf{x}} \tag{5}$$

where f_i, f_l, f_j, and f_k are the forces generated by the rotational spring for particles *i, l, j*, and *k*, respectively. Details related to the calculations of θ and *f* are presented in Appendix B.

For particle *i*, f_i is the only particle force generated by the rotational spring. The total internal spring force of particle *i* is equal to the sum of all the forces generated by all the springs related to it.

3.3. Particle force generated by a vertex contact

The initial configuration of the origami pattern considered in this study is the fully folded state; thus, the coordinates of many vertices are coincident. Although a vertex is initially displaced marginally to initiate unfolding, vertices mutually penetrate because of their dynamic response during the first few steps of unfolding. To ensure local non-intersection of the considered origami pattern, a contact model is used in the FPM to determine the vertex penetration and modify the particle motion.

As displayed in Fig. 3(c), the triangular panels *ijk* and *lkj* share the same crease *kj*. If particle *l* moves from *l* to *l′* and penetrates panel *ijk*, then the sign indicator η of the dihedral angle θ changes [see Eq. (B.1) in Appendix B]. After the penetration is determined, the contact force is calculated and applied in the opposite direction to modify the particle motion in the next time step. First, we define a virtual particle *l″* at the intersection of line *ll′* and panel *ijk* and allow it to represent panel *ijk* such that a point-to-surface collision changes to a point-to-point collision. The properties (mass, force, velocity, and displacement) of virtual particle *l″* are determined through the linear interpolation of the properties of particles *i, j*, and *k*.

Before and after a collision, particles *l* and *l″* satisfy the following basic equations of motion:

$$M_l \ddot{\mathbf{d}}_l = \mathbf{f}_l + \mathbf{f}_l^{\mathrm{con}} \tag{6a}$$

$$M_{l''} \ddot{\mathbf{d}}_{l''} = \mathbf{f}_{l''} + \mathbf{f}_{l''}^{\mathrm{con}} \tag{6b}$$

where M_l and $M_{l''}$ are the masses of particles *l* and *l″*, respectively; $\ddot{\mathbf{d}}_l$ and $\ddot{\mathbf{d}}_{l''}$ are the acceleration vectors of particles *l* and *l″*, respectively; $\mathbf{f}_l$ and $\mathbf{f}_{l''}$ represent the summations of particle force vectors for particles *l* and *l″*, respectively, and include the particle forces generated through bar

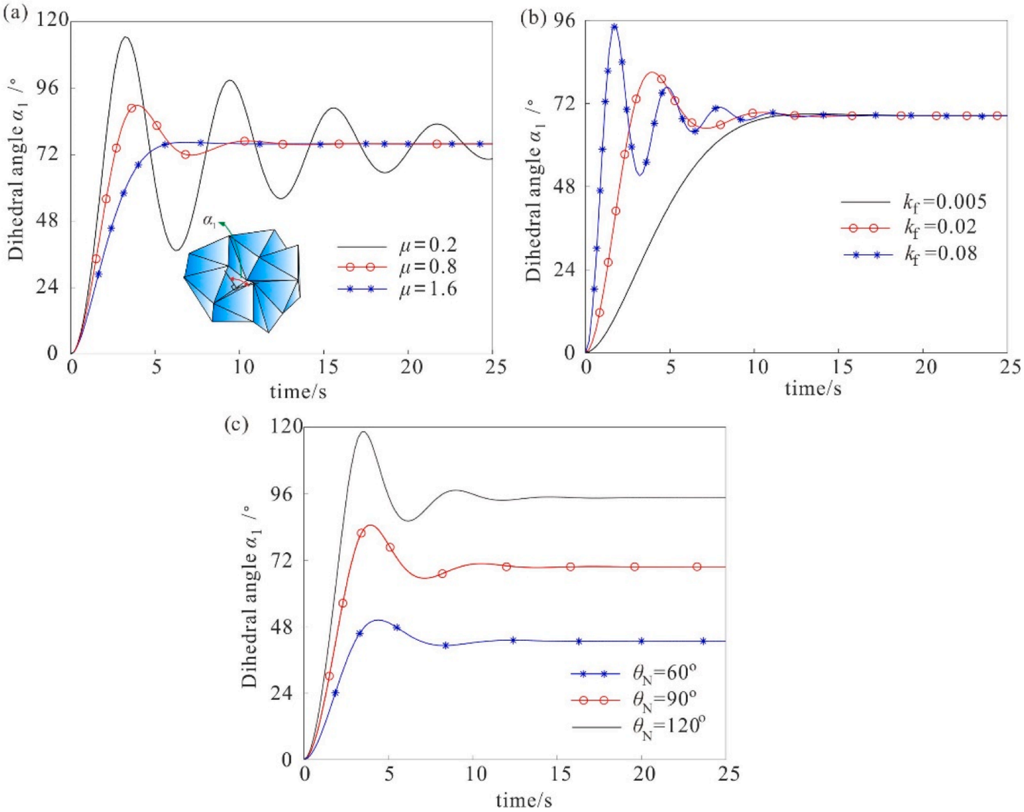

Fig. 5. Variations in the dihedral angle α_1 of the one loop Resch pattern with the neutral angle θ_N, the stiffness of the crease k_f, and the damping factor μ: (a) location of the dihedral angle α_1 in the considered origami pattern and the variation in α_1 with μ when $k_f = 0.02$ N/rad and $\theta_N = 90°$, (b) variation in α_1 with k_f when $\mu = 0.8$ and $\theta_N = 90°$ and (c) variation in α_1 with θ_N when $\mu = 0.8$ and $k_f = 0.02$ N/rad.

deformation, spring deformation, and damping; and $\mathbf{f}^{con}_l$ and $\mathbf{f}^{con}_{l''}$ are the contact force vectors of particles l and l'', respectively. Because particles l and l'' come into contact with each other, $\mathbf{f}^{con}_l = -\mathbf{f}^{con}_{l''}$.

On the basis of Eq. (2), a simple central difference is adopted to obtain the particle motion in Eq. (6). The parameters $\ddot{\mathbf{d}}_l$ and $\ddot{\mathbf{d}}_{l''}$ can be expressed as follows:

$$\ddot{\mathbf{d}}_l = \frac{\left(\mathbf{d}^l_{n+1} - \mathbf{d}^l_n\right) - \left(\mathbf{d}^l_n - \mathbf{d}^l_{n-1}\right)}{(\Delta t)^2} \tag{7a}$$

$$\ddot{\mathbf{d}}_{l''} = \frac{\left(\mathbf{d}^{l''}_{n+1} - \mathbf{d}^{l''}_n\right) - \left(\mathbf{d}^{l''}_n - \mathbf{d}^{l''}_{n-1}\right)}{(\Delta t)^2} \tag{7b}$$

When particle contact occurs in steps n and $n+1$, the penetration vector $\mathbf{g}_n$ can be determined from the displacements of particles l' and l'' as follows:

$$\mathbf{g}_n + \left(\mathbf{d}^l_{n+1} - \mathbf{d}^l_n\right) - \left(\mathbf{d}^{l''}_{n+1} - \mathbf{d}^{l''}_n\right) = 0 \tag{8}$$

When Eqs. (6)–(9) are combined, the contact forces for particle l and l' in step $n+1$ are expressed as follows:

$$\mathbf{f}^{con}_l = -\mathbf{f}^{con}_{l''} = \frac{M_l M_{l''}}{M_l + M_2}\left[\frac{\mathbf{f}_{l''}}{M_{l''}} - \frac{\mathbf{f}_l}{M_l} + \frac{\mathbf{g}_n - \left(\mathbf{d}^l_n - \mathbf{d}^l_{n-1}\right) + \left(\mathbf{d}^{l''}_n - \mathbf{d}^{l''}_{n-1}\right)}{(\Delta t)^2}\right] \tag{9}$$

Subsequently, $-\mathbf{f}^{con}_l$ is applied to particles l and l'. For particle l, $\mathbf{f}^{con}_l$ is the only particle force generated between particle l and l'. If contact occurs between particle l and other vertices, then additional contact forces must be applied to particle l.

3.4. Energy conservation in the FPM

In the FPM, explicit time integration is used to solve particle motion equations. When the Newmark time integration algorithm is used, energy conservation should occur during the dynamic unfolding of origami patterns [65–67]; thus, the energy released from the rotational springs (W_{rel}) should be equal to the summation of the other energy terms in the system, including the strain energy of the bar element (W_{strain}), the kinetic energy of the particle ($W_{kinetic}$), the damping work (W_{damp}), and the energy remaining in the spring after unfolding (W_{rem}). The energy stored, released, and remaining in the rotational springs of the entire origami pattern are labelled as W_{spr}, W_{rel}, and W_{rem}, respectively. The following equation is satisfied during the unfolding process:

$$\mathrm{W}_{rel} = \mathrm{W}_{strain} + \mathrm{W}_{kinetic} + \mathrm{W}_{damp} \tag{10}$$

Details related to the calculation of each energy term are presented in Appendix D.

4. Parameter analysis for origami pattern unfolding

The unfolding simulation algorithm used in the FPM is verified through an energy conservation study. Subsequently, the effects of the neutral angle (θ_N), the stiffness of the creases (k_f), and the damping factor (μ) on the unfolding process are analyzed.

We consider a model made from plastic laminate paper (for example, Durilla Premium Ice paper, 96lb cover, CTI Paper USA). To determine the material properties of this model, a material tension test is conducted (Appendix D.1). On the basis of the results of this test, the values of Young's modulus (E), thickness (h), and density (ρ) of the Ice paper are set as 1.30 GPa, 0.9 mm, and 320 g/m^2, respectively, in the simulation. To simplify the analysis, the neutral angles of the creases with initial dihedral angles of 90° and 120° are set as constant. Thus, these two types of creases are in equilibrium in the fully folded state. To test the effects of θ_N, k_f, and μ on the unfolding process for the crease with an initial dihedral angle of 0°, we set θ_N as 60°, 90°, and 120°; k_f as 0.005,

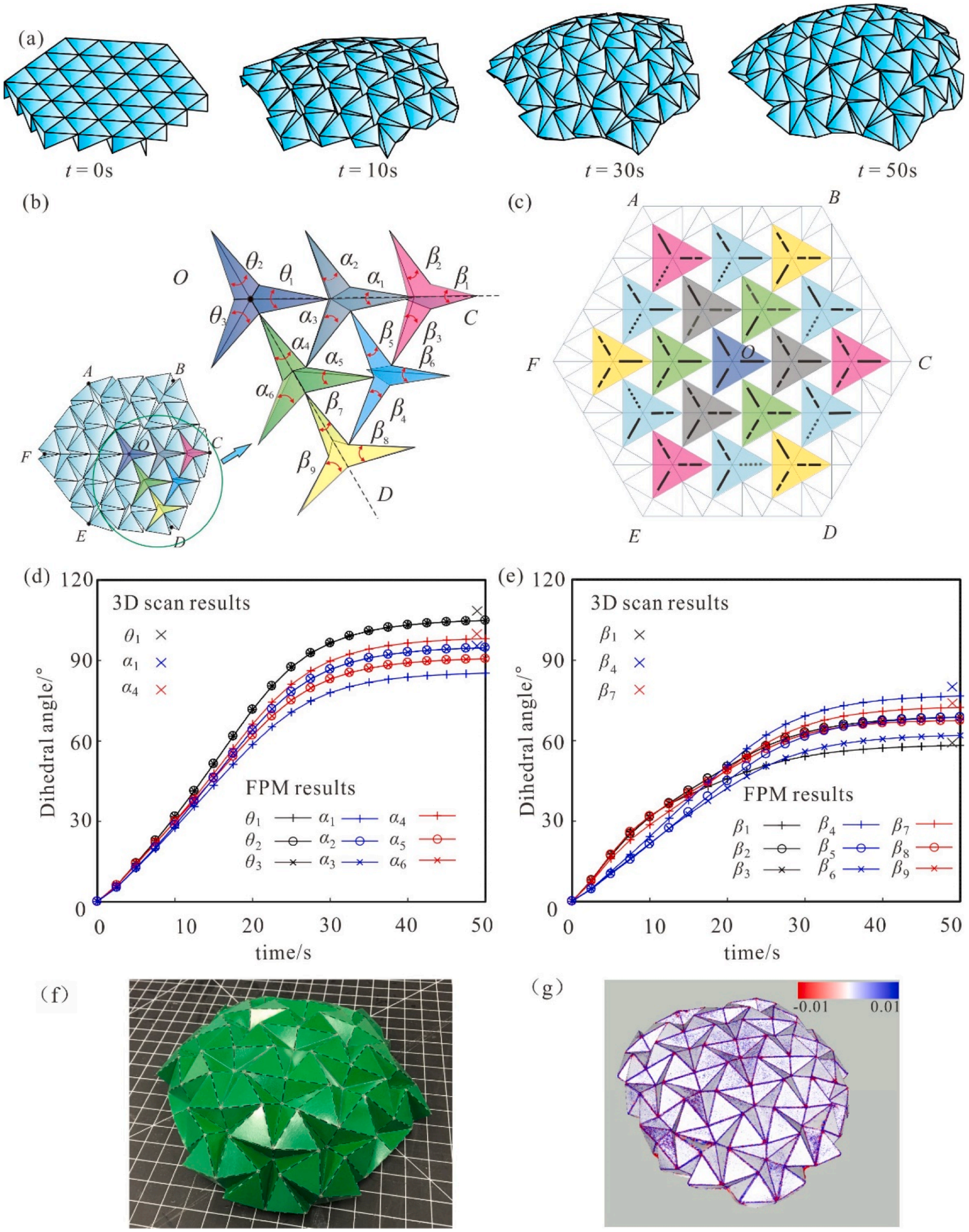

Fig. 6. (color online) Unfolding properties of the three-loop triangular Resch pattern. (a) Unfolding process of a triangular Resch pattern made from Ice paper ($\theta_N = 104.05^\circ$, $k_f = 0.1$ N/rad, and $\mu = 1.6$). (b) The dihedral angles we measured during the numerical unfolding process. (c) Symmetry of the three-loop triangular Resch pattern during the unfolding process. (d) Variations in the dihedral angles of the first and second loops of the three-loop triangular Resch pattern during the unfolding process. The corresponding experimental data is marked with a cross. (e) Variations in the dihedral angles of the third loop. (f) Physical model made from Ice paper and folded by hand. (g) Mean curvature map of the physical model.

0.02, and 0.08 N/rad; and μ as 0.2, 0.8, and 1.6. The side length of the equilateral triangle in the considered origami pattern is 30 mm, and the time step is set as 0.001 s.

Fig. 4 illustrates energy conservation in the one-loop triangular Resch pattern under different parameters. In each case, the released spring energy is equal to the summation of the kinetic energy, strain energy, and damping work, which verifies the accuracy of the algorithm used in the FPM. The strain energy in each case is equal to a very small value (approximately 10^{-5} N · m), which indicates that the origami pattern is subject to limited deformation. Thus, the analyzed origami pattern is relatively rigid. As the damping factor μ increases, the dynamic response decreases; however, the final remaining energy stored in the pattern is unchanged. As the stiffness k_f and neutral angle θ_N of the crease increase, the energy stored in the pattern increases; however, the ratio between the released spring energy and the remaining spring energy in the pattern remains largely unchanged.

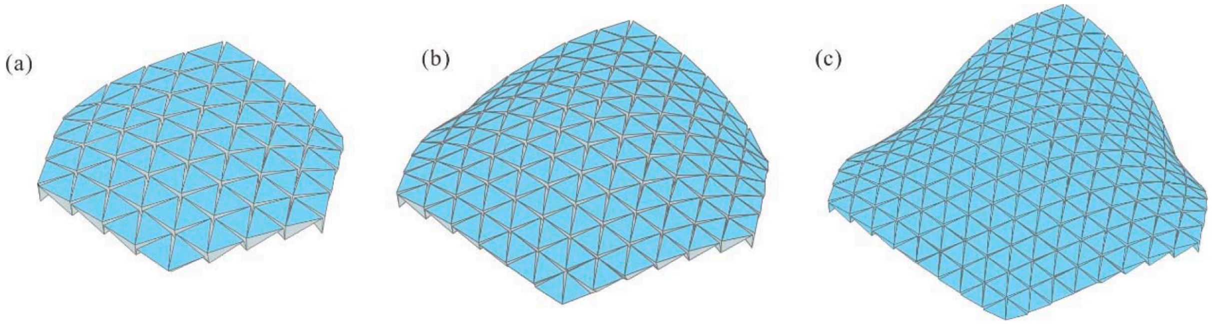

Fig. 7. Final shapes of triangular Resch patterns with a neutral angle (θ_N) of 60° unfolded by the energy stored in the creases: (a) four, (b) six, and (c) eight loops.

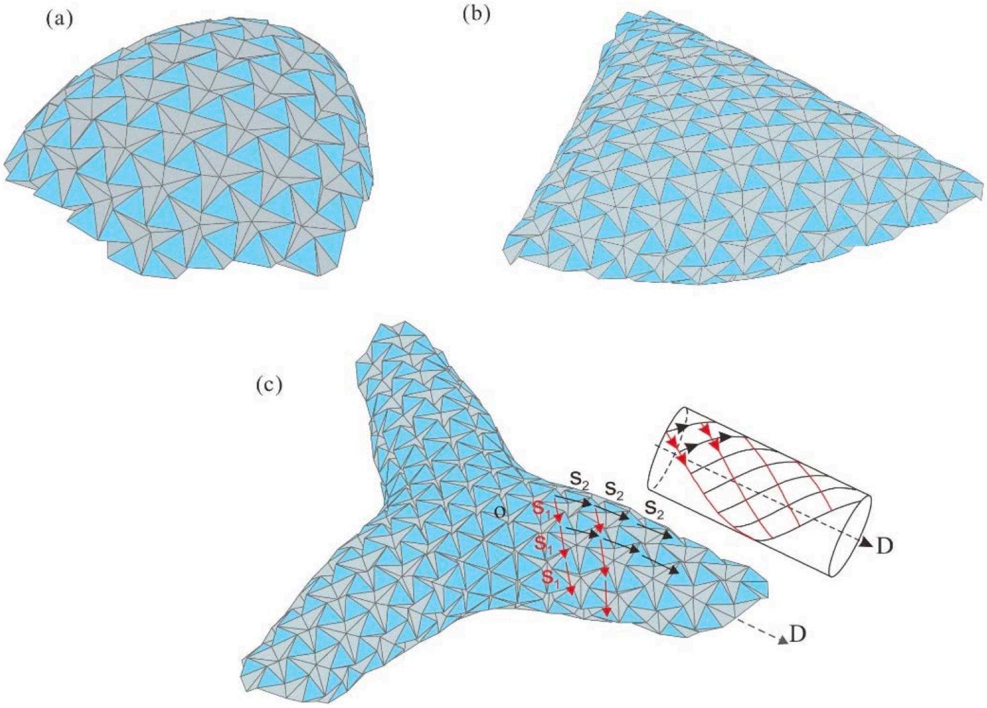

Fig. 8. Final shapes of triangular Resch patterns with a neutral angle (θ_N) of 120° unfolded by the energy stored in the creases: (a) four, (b) six, and (c) eight loops. (c) also shows the final cylindrical surface of the eight-loop triangular Resch pattern after unfolding, S1 and S2 represent two communitive screw motions which share a common axis OD.

Fig. 5 displays the variations in the dihedral angle α_1 at the center of the one-loop triangular Resch pattern with the neutral angle θ_N, the stiffness of the crease k_f, and the damping factor μ during the unfolding process. Although the neutral angle may have a certain intrinsic relationship with the crease stiffness, they are considered to be independent to simplify the analysis. As shown in Fig. 5, the damping factor and crease stiffness affect the velocity of the unfolding process but do not affect the final shape. In contrast, the neutral angle affects both the dynamic response and final configuration of the origami pattern. This result explains why the remaining energy does not differ for various damping factors. This also indicates that θ_N is the most crucial parameter for controlling the final shape of the triangular Resch pattern.

5. Unfolding and curvature programming

In this section, the motion properties of a three-loop triangular Resch pattern are first investigated by numerical simulation and experiment. Then, the final configurations of the triangular Resch patterns with four, six, and eight loops after free unfolding are obtained by FPM. At last, various curvatures are achieved by predefining the neutral angle and stiffness of the creases for the whole pattern.

5.1. Motion properties of the triangular Resch pattern with three loops

The unfolding process of a three-loop triangular Resch pattern is performed to reveal the motion properties and symmetry of this pattern. In the conducted simulation, this pattern is assumed to be made from Ice paper. The material properties of the simulated pattern are as follows: Young's modulus (E) = 1.30 GPa, thickness (h) = 0.9 mm, and density (ρ) = 320 g/m^2. Because the neutral angle and stiffness of the crease depend on the crease style and pattern material, a folding stiffness test and neutral angle test are conducted on the crease style in a physical model fabricated with the aforementioned pattern (Appendices C.2 and C.3). The folding stiffness k_f is 0.102 N/rad; the neutral angle is 104.05°; the damping factor is set as $\mu = 1.6$; and the time step Δt is set as 0.001 s. Fig. 6(a) illustrates the unfolding process of the three-loop triangular Resch pattern.

The variations in the dihedral angles displayed in Fig. 6(b) during the unfolding process in the FPM analysis are plotted in Figs. 6(d) and 9(e). The variations in the dihedral angles of other parts of the simulated

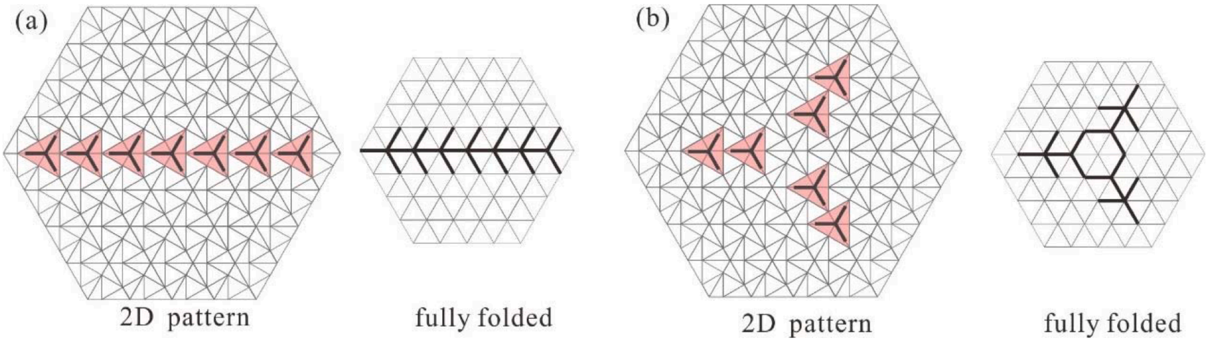

Fig. 9. Selected locations for controlling the crease properties of the three-loop triangular Resch pattern. (a) Tucks along one symmetry axis in the 2D unfolded pattern and fully folded pattern. The red color shows the middle tuck. The bold black line shows the location of the selected crease. (b) Six tucks along three symmetry axes in the 2D unfolded pattern and fully folded pattern.

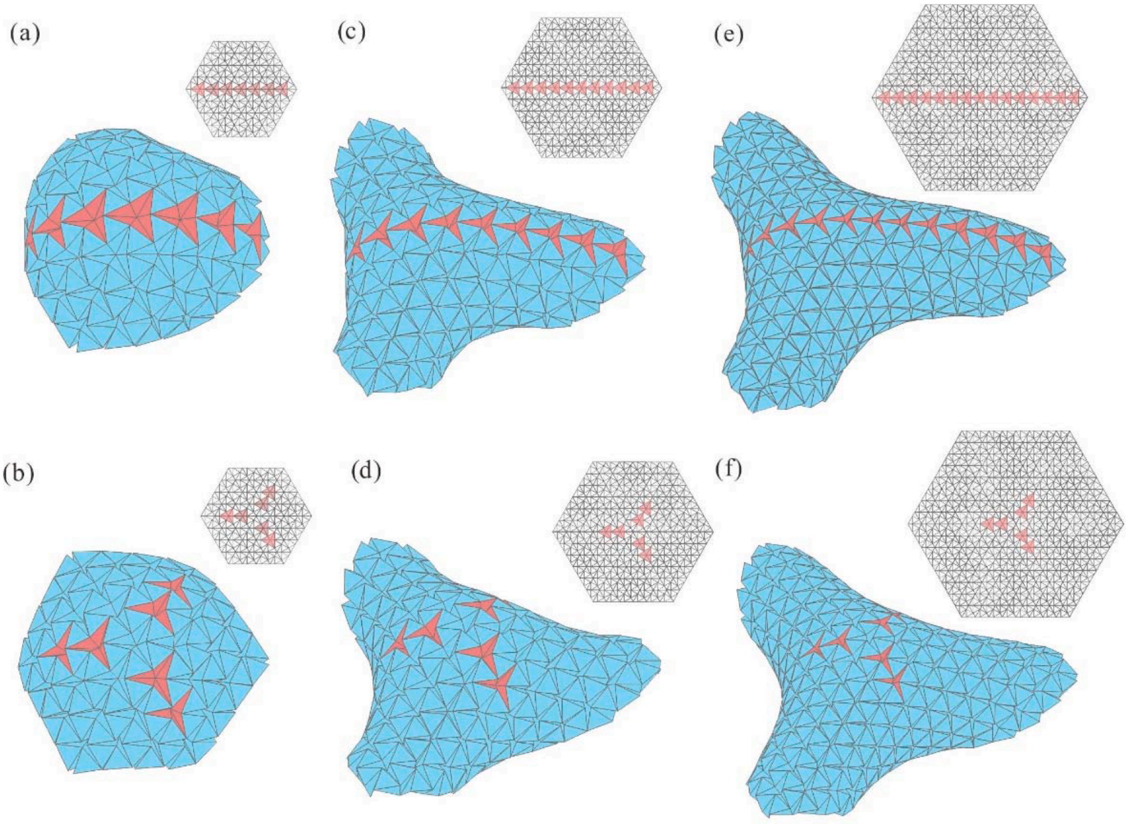

Fig. 10. (color online) Final shape of the triangular Resch pattern with different neutral angles after free unfolding: patterns obtained for (a) and (b) four, (c) and (d) six, and (e) and (f) eight loops. For the tucks marked in red, the neutral angle θ_N is 120°, and for the other tucks, the neutral angle θ_N is 60° The location of the neutral angle of 120° is indicated on the up-left corner of each subfigure.

origami structure are also examined, and the following distinctive characteristics are discovered for the three-loop triangular Resch pattern:

(1) Each loop has a unique configuration. Although the crease pattern is periodic, the natural configuration is not periodic and is different for every tuck in different loops. The dihedral angles gradually decrease from the first loop to the third loop, which leads to a natural domed shape for the final unfolded configuration. The dihedral angles outside the Vegreville Easter egg are equal, which explains why Resch and Christiansen (1970) could not fit the Vegreville Easter egg with the triangular Resch pattern.
(2) The three-loop triangular Resch pattern exhibits two groups of symmetry axes. OA, OC, and OE constitute the group 1 symmetry axes, and OB, OD, and OF constitute the group 2 symmetry axes. Because of these symmetry axes, the tucks with the same color in Fig. 6(c) have the same motion trajectory. Moreover, in each tuck, creases with the same line style have the same dihedral angles during the unfolding process.

We also fabricate a physical model of the three-loop triangular Resch pattern by using Ice paper (Fig. 6(f)); we use a laser system (PLS 6.75, Universal Laser Systems) to cut the paper. Subsequently, we use a handheld 3D scanner (Artec Spider Scanner, Artec 3D, Luxembourg) to capture the final shape achieved 30 min after the complete natural unfolding of the physical model. The adopted 3D scanner provides 3D images with resolution up to 0.1 mm. We measure the final values of the dihedral angles of the physical model and plotted the results in Fig. 6(d)

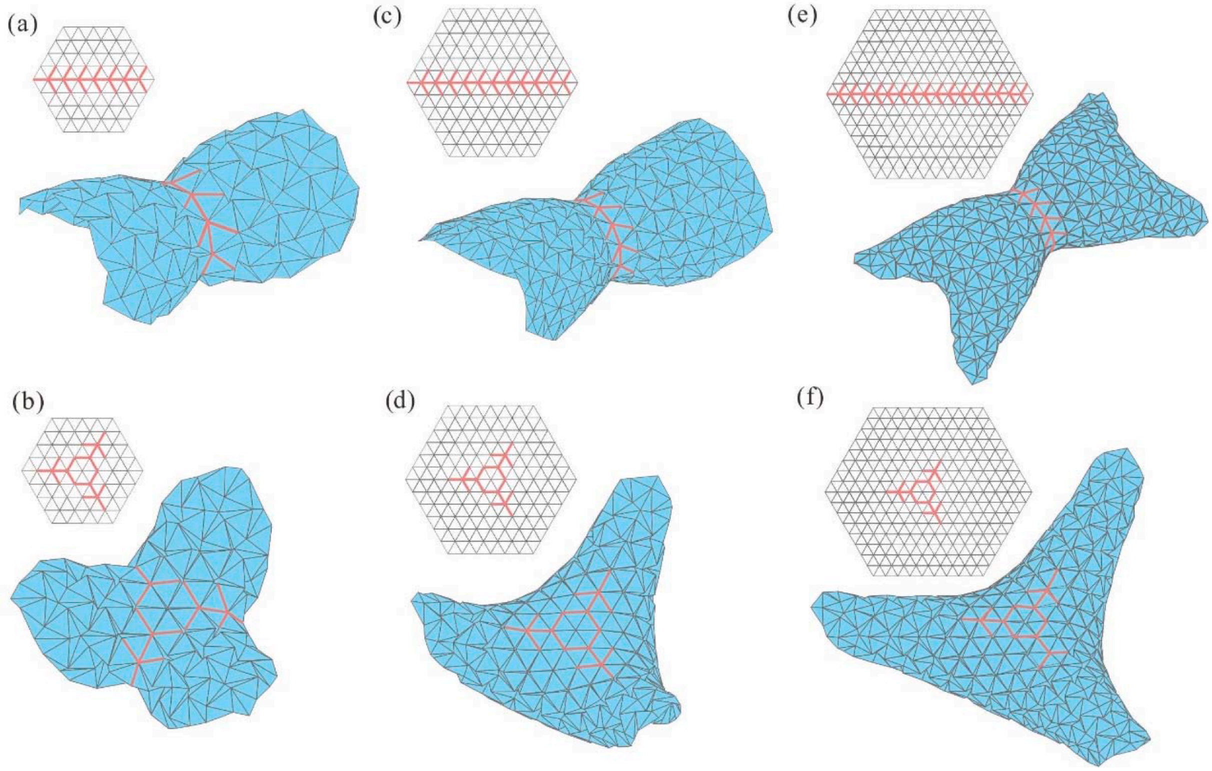

Fig. 11. (color online) Final shapes of the triangular Resch patterns with different constraints after free unfolding: patterns obtained (a) and (b) four, (c) and (d) six, and (e) and (f) eight loops. The tucks marked in red indicate the positions of the constraints. The neutral angle θ_N of other creases is 120° The location of the constrains is indicated on the up-right corner of each subfigure.

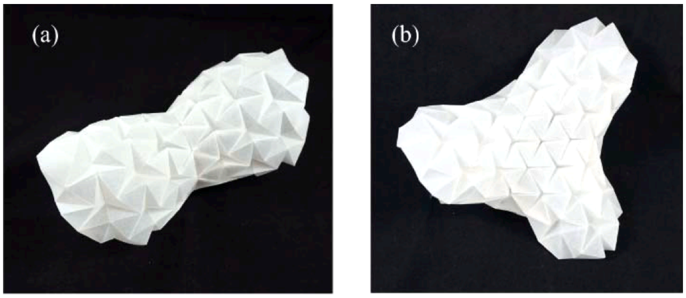

Fig. 12. Protypes of the final shapes of four-loop triangular Resch pattern models with different constraints after free unfolding: (a) model corresponding to the numerical results depicted in Fig. 11(a), and (b) model corresponding to the numerical results depicted in Fig. 11(b).

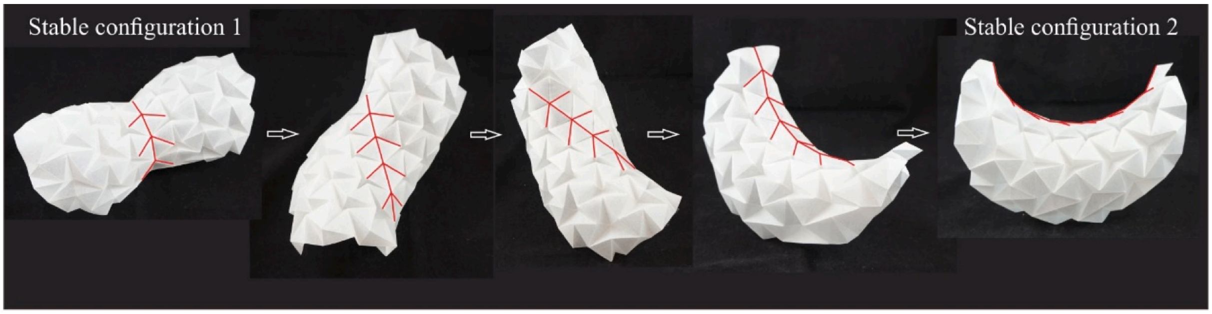

Fig. 13. Configurations obtained by twisting the four-loop triangular Resch pattern with constraints along one symmetry axis. The bold red line shows the position of the constrains. Because the three middle configurations are unstable, tapes and clips are used to stabilize these configurations for capturing their photos.

and (e).

The measured and simulated dihedral angles are approximately equal. The small difference between the measured and simulated results might have originated from the deformation of the physical model. To visualize the deformation of this model, we compute the mean curvature of the scanned final shape. As displayed in Fig. 6(g), the mean curvature

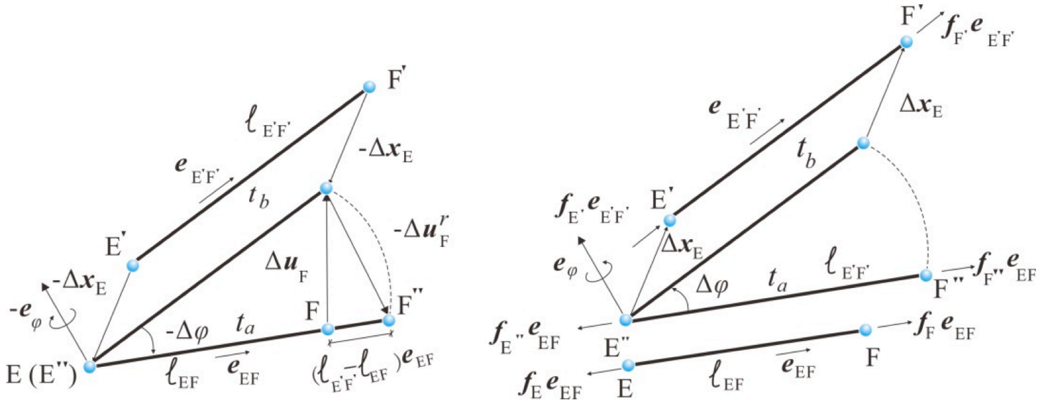

(a) reversed motion (b) forward motion

Fig. A.1. Illustration of the fictitious motion.

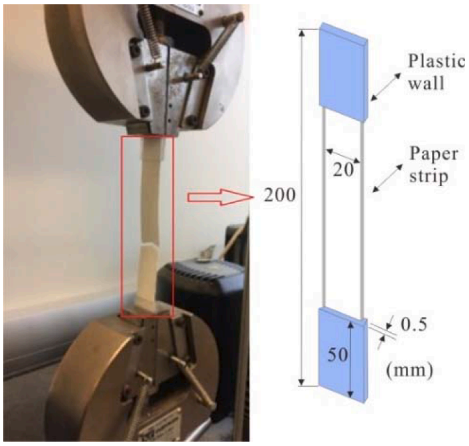

Fig. D.1. Tension test on paper material using the Instron machine.

Table D.1
Material properties for Ice paper.

E (MPa)	k_f (N.mm)/mm/rad	θ_N (degree)
1317.05	0.0843	116.86°
1323.50	0.1253	103.44°
1298.31	0.0995	100.57°
1277.20	0.1103	105.57°
1296.98	0.0950	93.80°
Average		
1302.61	0.1020	104.05°

in all creases is much larger than that in the panels, which indicates the obvious deformation of the creases in the physical model. We also observe a high mean curvature in some panels of the physical model, which indicated that the paper panels are deformed in the folding process. Thus, the difference in the rigidity of the numerical model (rigid) and physical model (non-rigid) leads to the difference between the numerical and experimental results.

5.2. Natural curvature of the triangular Resch pattern after unfolding

Subsequently, we investigated triangular Resch patterns with four, six, and eight loops. As displayed in Figs. 7 and 8, when the neutral angle θ_N is 60°, the final shapes of these three patterns are similar. However, when θ_N is 120°, the final shapes of these patterns are considerably different. When θ_N is 120°, the final shape of the four-loop triangular Resch pattern is a dome-like shape. As the number of loops increases further, the pattern begins curling inward. When the triangular Resch pattern has four or six loops, the final shape exhibits only positive curvature. However, when this pattern contains eight loops, the final shape shows positive and negative curvature. Thus, the shape of the triangular Resch pattern after unfolding cannot be scaled by adding loops.

Tachi [33] reported that if periodic rigid folding occurred, then the folded form generally approximated a cylindrical surface. In Fig. 8(c), which depicts the final cylindrical surface of the eight-loop triangular Resch pattern after unfolding, $\mathbf{S}_1$ and $\mathbf{S}_2$ represent two communitive rigid transformations, that is, two screw motions. These screw motions share a common axis, OD, and thus result in the formation of an approximately cylindrical surface whose axis is located on the common axis. Because the triangular Resch pattern contains three symmetry axes, as the pattern becomes larger, its final shape tends to comprise three symmetric cylinders. Thus, the numerical simulation results agree with the mathematical proof.

5.3. Curvature programming

Because different neutral angles result in different final unfolded shapes of the triangular Resch pattern, we posit that the final unfolded shape will be programmed by controlling the neutral angles of the creases at different locations. Two methods are proposed for programming the curvature of the unfolded shape of the triangular Resch pattern: (1) making the neutral angles of selected creases larger than those of others, which results in the pattern having a larger local opening, and (2) adding constraints to selected creases at the beginning of the unfolding process, which prevents the local unfolding of the pattern at certain points.

As displayed in Fig. 1(c), the fully folded Resch pattern contains three initial angles: 60°, 90°, and 120° To achieve prominent curvature changes, three creases with an initial angle of 0° in the same tuck are regarded as a group, and crease properties are modified only by group, as depicted in Fig. 9. Although different crease groups can increase or limit the unfolding of a pattern, the intrinsic geometry of the triangular Resch pattern limits the choice of crease group. Boundary units play a crucial role in constraining the triangular Resch pattern [31,68]; however, they do not considerably affect the curvature in the middle of the pattern. The addition of arbitrary constraints inside the triangular Resch pattern may lock the pattern in a single configuration. Therefore, the property change of the crease must follow the motion coordination of the triangular Resch pattern. Magliozzi et al. [57] discovered a general rule that if a unit is surrounded by three constrained units, then this unit is constrained. If this rule is employed, then no redundant constraints are added to the triangular Resch pattern.

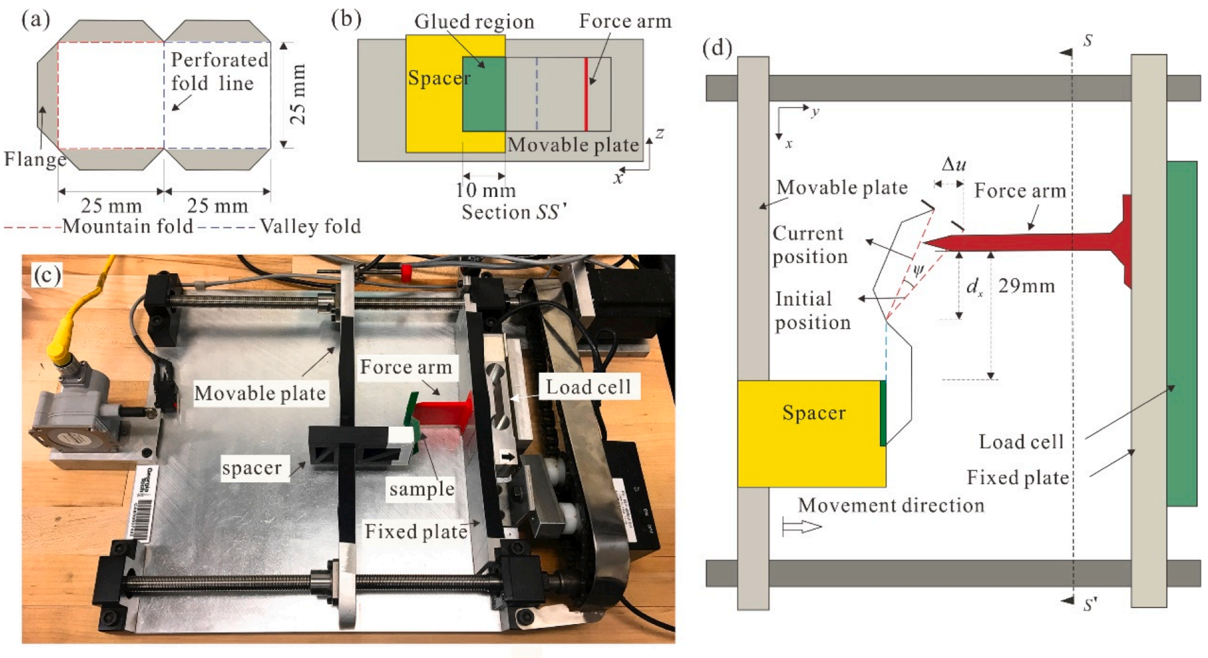

Fig. D.2. Folding stiffness test. (a) and (b) characterization of the folding stiffness of the perforated crease; (c) and (d) the custom-built mechanical testing bed.

On the basis of the aforementioned information, locations are selected using two methods for programming the curvature of the triangular Resch pattern. The first method involves selecting all the tucks only along one symmetry axis, which breaks the three-axis symmetry of the triangular Resch pattern, as shown in Fig. 9(a). The second method involves selecting six tucks in the middle part of the triangular Resch pattern, which control the middle part of the pattern according to Magliozzi et al. [57] rule, as shown in Fig. 9(b).

Fig. 10 shows the final shapes of the triangular Resch patterns with four, six, and eight loops after free unfolding when controlling the neutral angles of the selected creases. The neutral angle of the creases in the selected tucks is set as 120°, and all the other neutral angles are set as 60° The creases with a larger neutral angle release more energy than do the other creases and locally increase the curvature of the triangular Resch pattern. The selected tucks with a large opening are connected to other tucks, and under the influence of the selected tucks, the other tucks are unfolded more than before. Consider the triangular Resch pattern with eight loops as an example. The final shape of this pattern depicted in Fig. 10(e) contains a “whale tail” and only one symmetry axis, whereas the final shape of this pattern depicted in Fig. 10(f) contains three symmetric cylinders in the middle. The final shapes in Fig. 10 are notably different from those in Figs. 7 and 8, which indicates the programmability of the curvature of the triangular Resch pattern.

Fig. 11 illustrates the final shapes of the triangular Resch pattern with four, six, and eight loops after unfolding when the unfolding of the creases was constrained in the selected tucks. In this case, the neutral angle of the unconstrained creases is 120° Because a higher neutral angle results in the release of more energy in the unfolding process, adding the constraints to creases limits the opening of relevant panels. As displayed in Fig. 11, the addition of constraints along one symmetry axis leads to the triangular Resch pattern with the final shape of a simplified “butterfly”, which contains a circle in the middle with one wing at each side [Fig. 11(a),(c), and (e)]. The addition of constraints along three symmetry axes results in the triangular Resch pattern with a final shape that contains three saddle joints in the middle [Fig. 11(b),(d), and (f)].

Fig. 12 displays two prototypes of four-loop triangular Resch models with different constraints. These models are made from Ice paper, which is cut using the adopted laser system and manually folded. Clips are used to limit the unfolding of the two panels on both sides of the selected crease. It is noted that the adopted numerical model is rigid, whereas the adopted physical models are not rigid; therefore, we only qualitatively compare the experimental and numerical results. The shapes of the physical models displayed in Fig. 12 are highly similar to the corresponding numerical results depicted in Fig. 11(a) and (b).

A different stable configuration of the prototype displayed in Fig. 12 (a) can be obtained by twisting it (Fig. 13). We measure all the dihedral angles between the open panels in each tuck of this prototype in the two stable configurations. The summation of the dihedral angles for Stable configuration 1 and Stable configuration 2 depicted in Fig. 13 are 66.76 and 62.71 rad, respectively. The summation of the dihedral angles for Stable configuration 1 is higher than that for Stable configuration 2, which indicates that the remaining energy of configuration 1 is lower than that of configuration 2. The numerical simulation indicated that the unfolding process results in the direct formation of a stable configuration with lower energy.

6. Conclusion

This study uses the FPM to simulate the unfolding of the triangular Resch pattern. Instead of using external forces or displacements, the unfolding of the aforementioned pattern is triggered only by the energy stored in its creases. Comparing with our precious work on the analysis of origami structures, the new contents include introducing a contact model in the FPM to ensure local non-intersection during the unfolding process of the triangular Resch pattern, investigating the key parameters on the unfolding process of this pattern, revealing the natural unfolding properties of this pattern, and programming this pattern to naturally achieve surfaces with various curvatures. A comparison between the experimental and numerical results confirmes the accuracy of the proposed numerical method.

The simulation results for the unfolding of the triangular Resch pattern indicate that the natural configuration of this pattern is complex and depended on many factors. The motions of each loop in this pattern are completely different. As the triangular Resch pattern becomes larger, its natural shape after unfolding changes from a dome-like shape to a shape in which three cylinders intersected at the center. Thus, the final shape of the triangular Resch pattern after unfolding cannot be scaled through the addition of concentric loops. This finding explains why Ron Resch failed to fold this pattern to fit the shape of an Easter egg in 1970. Notably, rather than the crease stiffness or damping factor, the neutral angle is the most crucial parameter affecting the final shape of the triangular Resch pattern after unfolding. Although the neutral angle may has a certain intrinsic relationship with the crease stiffness, we consider them to be independent in the present study.

By changing the neutral angle and adding constraints, the original symmetry of the triangular Resch patterns is broken. We could program the final curvature after unfolding such that the final shape is comprised of positive and negative curvatures. Because diverse locations can be employed in the triangular Resch pattern when performing modifications, the programming of the curvature results in various final pattern shapes. The results of this study indicate that different curvatures can be achieved through the continuous unfolding of the triangular Resch pattern. The experimental results obtained for fabricated prototypes indicate that the remaining energy of the final configuration obtained in the numerical analysis is lower than that of other stable configurations. However, it is difficult to make a precise rigid physical model with different neutral angle, which will be considered in the future. This paper only focuses on the natural shape achieved after unfolding and the possibility of programming the curvature of the triangular Resch pattern. The inverse problem of fitting a shape with a modified triangular Resch pattern will be investigated in a future study.

CRediT authorship contribution statement

Ying Yu: Data curation, Writing – review & editing. **Yan Chen:** Investigation, Writing – review & editing. **Glaucio Paulino:** Investigation, Writing – review & editing.

Declaration of Competing Interest

The authors declare that they have no known competing financial interests or personal relationships that could have appeared to influence the work reported in this paper.

Data Availability

Data will be made available on request.

Acknowledgments

We thank Prof. Emily Daniels Sanders for helpful comments and input, which contributed to substantial improvements of the manuscript. The authors gratefully acknowledge the financial support provided by the US National Science Foundation (No. 1538830), Natural Science Foundation of China (Nos. 51825503, 51721003 and 52238001), Science and Technology Plan of Guangdong, China (No. 210715156881741), and the China Scholarship Council (No. 201706515032). We also acknowledge the Margareta Engman Augustine Professor of Engineering at Princeton University. The information provided in this manuscript is solely by the authors and does not necessarily reflect the views of the sponsors or sponsoring agencies.

Appendix A. Particle internal force generated by bar deformation

Particles are connected by bar elements. Once a particle moves, the displacement of the particle leads to rigid body motion and deformation of the bars connected to the particle. Although we focus on rigid origami in this work, the bar-and-particle model can simulate both rigid and non-rigid origami. Using the fictitious motion procedure [51], the rigid body motion and pure deformation of the bar can be separated from the particle displacement, which results in the successful handling of geometric nonlinearity in the FPM.

To calculate the internal force of particles E and F generated by bar EF, Fig. A.1 illustrates the fictitious motions procedure of bar EF from time t_a to time t_b. Time t_a is taken as the reference configuration. To remove the rigid body motion of bar EF, first, we assume that bar E′F′ at time t_b has a fictitious translation ($-\Delta x_{\mathrm{E}}$) and a fictitious reversed rotation ($-\Delta\varphi$). The parameters Δx_{E} and $\Delta\varphi$ are the relative displacements and rotations of particle E within the time step Δt, respectively. Then, bar E′F′ is displaced to position E″F″, as shown in Fig. A.1(a). The internal force of MN is calculated at this configuration. The incremental deformation displacement of EF,$\Delta\mathbf{u}_{\mathrm{F}}^{\mathrm{d}}$, can be determined by [69]:

$$\Delta\boldsymbol{u}_{\mathrm{F}}^{\mathrm{d}} = \Delta\boldsymbol{u}_{\mathrm{F}} + \Delta\boldsymbol{u}_{\mathrm{F}}^{\mathrm{r}} = \Delta\boldsymbol{u}_{\mathrm{F}} - \left(\boldsymbol{R}^{T} - \boldsymbol{I}\right)d\boldsymbol{x}' \tag{A.1}$$

where $\Delta\boldsymbol{u}_{\mathrm{F}}^{\mathrm{d}}$ is the relative displacement between particles E and F, and $\Delta\boldsymbol{u}_{\mathrm{F}}^{\mathrm{r}}$ is the relative rigid body displacement caused by the fictitious rotation. I is a 3×3 unit matrix; R is the rotation matrix of $\Delta\varphi$; and $d\mathbf{x}'$is the position vector of particle F in the local deformation coordinate at time t_b. $d\mathbf{x}' = [\ell_{\mathrm{E'F'}} \quad 0 \quad 0]^{\mathrm{T}}$, where $l_{\mathrm{E'F'}}$ is the length of bar EF at time t_b. For the bar element, the deformation is only related to the variations in the bar length. Instead of Eq. (A.3), we determine the incremental deformation of the bar element by using the following equation:

$$\Delta\boldsymbol{u}_{\mathrm{F}}^{\mathrm{d}} = (\ell_{\mathrm{E'F'}} - \ell_{\mathrm{EF}})\boldsymbol{e}_{\mathrm{EF}} \tag{A.2}$$

where ℓ_{EF} is the length of element EF at t_a, and e_{EF} is the directional vector of element EF at time t_a.

Because element E″F″ is parallel to element EF (Fig. A.1(b)), the axial force of element $\mathbf{f}_{\mathrm{F''}}$ can be given as follows:

$$\mathbf{f}_{\mathrm{F''}} = -\mathbf{f}_{\mathrm{E''}} = \left[\sigma_a A_a + \frac{E_a A_a}{l_{\mathrm{EF}}}(\ell_{\mathrm{E'F'}} - \ell_{\mathrm{EF}})\right]\mathbf{e}_{\mathrm{EF}} \tag{A.3}$$

where E_a is Young’s modulus, σ_a is the axial stress at t_a, and A_a is the cross-sectional area.

Finally, let the element E″F″ be subject to a translation Δx_{E} and rotation $\Delta\varphi$ to regain its original position. The real axial force of element $\mathbf{f}_{\mathrm{F'}}$ is obtained using the following equation:

$$\mathbf{f}_{\mathrm{F'}} = -\mathbf{f}_{\mathrm{E'}} = \left[\sigma_a A_a + \frac{E_a A_a}{l_{\mathrm{EF}}}(\ell_{\mathrm{E'F'}} - \ell_{\mathrm{EF}})\right]\mathbf{e}_{\mathrm{E'F'}} \tag{A.4}$$

where $\mathbf{e}_{\mathrm{E'F'}}$ is the directional vector of EF at t_b, and $\mathbf{f}_{\mathrm{F'}}$ is the element internal force applied to particle F. This is only the particle force generated from the deformation of bar EF. The total internal force of particle F should be determined from the contribution of all bars connected to it.

Appendix B. Calculation of the dihedral angle and its gradient

The dihedral angle θ in Eq. (9) can be determined by the following equations [42]:

$$\theta = \eta \arccos\left(\frac{\mathbf{m}\cdot\mathbf{n}}{\| \mathbf{m} \| \| \mathbf{n} \|}\right) \tag{B.1 a}$$

$$\eta = \begin{cases} \operatorname{sgn}(\mathbf{m}\cdot\mathbf{r}_{k\ell}) & \mathbf{m}\cdot\mathbf{r}_{k\ell} \neq 0 \\ 1, & \mathbf{m}\cdot\mathbf{r}_{k\ell} = 0 \end{cases} \tag{B.1 b}$$

where η is the sign indicator of the dihedral angle θ; **m** and **n** are the normal vectors perpendicular to panels *ikj* and *kℓj*; $\mathbf{m} = \mathbf{r}_{ij} \times \mathbf{r}_{k\ell}$, and $\mathbf{n} = \mathbf{r}_{kj} \times \mathbf{r}_{k\ell}$; and $\mathbf{r}_{pq}$denotes a vector connecting any two particles (*p* and *q* refer to the labels of any pair of nodes, ℓ or *k*).

Based on the distance vector and simplifying transformations [70], the gradients of dihedral angle θ without singularities in the numerical analysis can be expressed as [42]:

$$\frac{\partial\theta}{\partial\mathbf{x}_i^{(r)}} = \frac{\| \mathbf{r}_{kj} \|}{\| \mathbf{m} \|^2}\mathbf{m} \tag{B.2 a}$$

$$\frac{\partial\theta}{\partial\mathbf{x}_l^{(r)}} = \frac{\| \mathbf{r}_{kj} \|}{\| \mathbf{n} \|^2}\mathbf{n} \tag{B.2 b}$$

$$\frac{\partial\theta}{\partial\mathbf{x}_j^{(r)}} = \left(\frac{\mathbf{r}_{ij}\cdot\mathbf{r}_{kj}}{\| \mathbf{r}_{kj} \|^2} - 1\right) \frac{\partial\theta}{\partial\mathbf{x}_i^{(r)}} - \frac{\mathbf{r}_{kl}\cdot\mathbf{r}_{kj}}{\| \mathbf{r}_{kj} \|^2} \frac{\partial\theta}{\partial\mathbf{x}_l^{(r)}} \tag{B.2 c}$$

$$\frac{\partial\theta}{\partial\mathbf{x}_k^{(r)}} = \left(\frac{r_{kl}\cdot r_{kj}}{\| r_{kj} \|^2} - 1\right) \frac{\partial\theta}{\partial\mathbf{x}_l^{(r)}} - \frac{r_{ij}\cdot r_{kj}}{\| r_{kj} \|^2} \frac{\partial\theta}{\partial\mathbf{x}_i^{(r)}} \tag{B.2 d}$$

Appendix C. Energy calculation

The energy stored, released, and remaining in the rotational springs of the whole origami pattern are labelled as W_{spr}, W_{rel} and W_{rem}, respectively.

$$W_{\text{spr}} = \sum_{i=1}^{i=nc} k_i \ell_i \theta_{\text{N}i}^2 \tag{C.1}$$

$$W_{\text{rel}} = \sum_{i=1}^{i=nc} k_i \ell_i \left(\theta_{\text{N}i}^2 - (\theta_{\text{N}i} - \theta_i)^2\right) \tag{C.2}$$

$$W_{\text{rem}} = \sum_{i=1}^{i=nc} k_i \ell_i (\theta_{\text{N}i} - \theta_i)^2 \tag{C.3}$$

where *nc* is the number of creases and k_i, ℓ_i, $\theta_{\text{N}i}$ and θ_i are the stiffness, length, neutral angle, and present dihedral angle of crease *i*, respectively.

The strain energy $W_{\text{strain}}$is attributed to the deformation of the bars connected to the particles,

$$W_{\text{strain}} = \frac{1}{2}\sum_{j=1}^{j=nb} \int \sigma_j \varepsilon_j dV_j \tag{C.4}$$

where *nb* is the number of bars and σ_j, ε_j and V_j are the stress, strain and volume of bar *j*, respectively.

The kinetic energy $W_{\text{kinetic}}$is attributed to the particle velocity,

$$W_{\text{kinetic}} = \frac{1}{2}\sum_{q=1}^{q=np} m_q {v_q}^2 \tag{C.5}$$

where *np* is the number of particles and m_q and $v_q$are the mass and velocity of particle *q*, respectively.

The damping work W_{damp} is attributed to the artificial damping force on each particle,

$$W_{\text{damp}} = \sum_{q=1}^{q=np} \mu m_q v_q \tag{C.6}$$

Appendix D. Experiment

D.1. *Stiffness under tension*

A laser machine (PLS 6.75, Universal laser systems) is used to fabricate the samples from the Ice paper. To obtain Young's modulus E of the Ice paper, an Instron model 5566 equipped with a 30 kN load cell is used to perform tensile tests on five samples (see Fig. D.1) of each material. Each sample made of Ice paper has dimensions of 20 mm × 100 mm with a thickness of 0.9 mm. The value of Young's modulus of each paper is taken as the average of five samples. The experimental data are collected in Table D.1.

D.2. *Folding stiffness*

For each kind of paper, the folding stiffness k_f of a crease is determined as the average of five samples computed from a folding stiffness test. Each sample is composed of two square panels of dimensions 25 mm × 25 mm, jointed by a perforated crease line (see Fig. D.2 (a) and (b)). The samples are surrounded by folded flanges that simulated the presence of the neighbouring panels in an origami system. A custom-built mechanical testing bed is used to measure crease stiffness [43], as shown in Fig. D.2(c) and (d). First, we attach a spacer to the movable plate. This spacer holds the sample while leaving clearance for the free end of the sample to displace freely in space to some extent. Second, we mount a 3D-printed force arm to the fixed plate with its center offset 29 mm from the spacer edge. This arm transmits the reaction force from the sample to the load cell.

The moment (M) at the crease lines and the rotational angle (ψ) are calculated as follows:

$$M = F_0 d_x \tag{D.1 a}$$

$$\psi = \tan^{-1}\left(\frac{u_0}{d_x}\right) - \tan^{-1}\left(\frac{u_0 - \Delta u}{d_x}\right) \tag{D.2 b}$$

where d_x is the distance between the crease line and the force arm (i.e., $d_x = 19$ mm), $\boldsymbol{F_0}$ is the measured force from the load cell, and u_0 is the initial distance between the force arm and the spacer in the y-direction. For the measurements of folding stiffness, we observe different initial neutral angles after a complete fold. In such cases, u_0 is measured for each sample based on where the force arm touched the sample. The results of the folding stiffness are listed in Table. D.1.

D.3. *Neutral angle test*

As shown in Fig. 6(b), the neutral angle θ_N for a simple crease is the dihedral angle between its two panels when the simple fold is in a natural equilibrium state. The neutral angle θ_N of a fold is a complex function of the folding history, applied load and properties of the materials [71]. Five samples are prepared from Ice paper. The sample dimensions are the same as in the folding stiffness test, as shown in Fig. D.2(a). When manufacturing a model, we try to follow the same folding procedure each time. Then, fully folded models are allowed to unfold naturally based on the energy stored in the creases. After 30 min, when the models are in equilibrium, the angles of the folds are calculated using the law of cosines.

The time-dependant behavior of the creases is not considered here. We take the average of the results from the five samples. As shown in Table D.1, the neutral angle for Ice paper is 104.05°

Appendix E. Nomenclature

m_α	mass of particle α
$\ddot{\mathbf{d}}_\alpha$	acceleration vector of particle α
$\mathbf{f}_\alpha^{\mathrm{int}}$	particle internal force vector generated by the deformation of bars
$\mathbf{f}_\alpha^{\mathrm{spr}}$	particle force vector generated by the deformation of rotational springs
$\mathbf{f}_\alpha^{\mathrm{dmp}}$	damping force vector of particle α
$\mathbf{f}_\alpha^{\mathrm{cont}}$	contact force vector applied to particle α
$\mathbf{g}_n$	penetration vector
$U_{\mathrm{spr}}^{\mathrm{int}}$	stored energy of the rotational spring
θ	dihedral angle
E	Young's modulus
H	thickness of the paper
P	density of the paper
k_f	Folding stiffness
θ_N	Neutral angle
μ	damping factor
Δt	time step
W_{spr}	energy stored in the rotational springs
W_{rel}	released by the rotational springs
W_{rem}	remaining in the rotational springs
W_{strain}	strain energy
W_{kinetic}	kinetic energy
W_{damp}	damping work

References

[1] Ghys E. Sur la coupe des v̂etements: variation autour d’un th`eme de Tchebychev. L’Enseign Math́ematique 2011;57:165–208.

[2] Li MZ, Cai ZY, Sui Z, Yan QG. *Multi-point forming technology for sheet metal*. Materials Processing Technology 2002;129:333–8. https://doi.org/10.1016/s0924-0136(02)00685-4. 129(1-3).

[3] Ma C, Chen C, Xu Z, Lv C, Zheng Q. Substrate curvature dependence of intrinsic contact angles. Extrem Mech Lett 2021;48:101388. https://doi.org/10.1016/j.eml.2021.101388.

[4] Suzuki S, Ohtake Y, Suzuki H. Curvature gradient-estimation using CT sinogram and its application to reverse engineering. Comput Aided Des 2022;148:103240. https://doi.org/10.1016/j.cad.2022.103240.

[5] Yang Y, Qiao H, Lu Y, Zhao J, Sun B. The saturated convex bending curvature of 7075 aluminum panel bent by orthogonal laser shock forming. Opt Laser Technol 2022;156:108586. https://doi.org/10.1016/j.optlastec.2022.108586.

[6] Callens SJP, Zadpoor AA. From flat sheets to curved geometries: origami and kirigami approaches. Mater Today 2018;21:241–64. https://doi.org/10.1016/j.mattod.2017.10.004.

[7] Fonseca LM, Rodrigues GV, Savi MA. An overview of the mechanical description of origami-inspired systems and structures. Int J Mech Sci 2022;223:107316. https://doi.org/10.1016/j.ijmecsci.2022.107316.

[8] Lang RJ, Howell L. Rigidly Foldable quadrilateral meshes from angle arrays. J Mech Robot 2018;10:021004. https://doi.org/10.1115/1.4038972.

[9] Miyashita S, Guitron S, Li S, Rus D. Robotic metamorphosis by origami exoskeletons. Sci Robot 2017;2:eaao4369. https://doi.org/10.1126/scirobotics.aao4369.

[10] Morris E, McAdams DA, Malak R. The state of the art of origami-inspired products: a review. Vol. 5B. In: Proceedings of the 40th Mechnical Robotics Conference. Charlotte, North Carolina, USA: American Society of Mechanical Engineers; 2016. https://doi.org/10.1115/DETC2016-59629. V05BT07A014.

[11] Peraza-Hernandez EA, Hartl DJ, Malak Jr RJ, Lagoudas DC. Origami-inspired active structures: a synthesis and review. Smart Mater Struct 2014;23:094001. https://doi.org/10.1088/0964-1726/23/9/094001.

[12] Han X, Li L, Mei C, Hu Y, Wang X. Acoustic source localization in three-dimensional space based on acoustic valley-Hall topological insulators. Int J Mech Sci 2022;217:107048. https://doi.org/10.1016/j.ijmecsci.2021.107048.

[13] Pratapa PP, Suryanarayana P, Paulino GH. Bloch wave framework for structures with nonlocal interactions: application to the design of origami acoustic metamaterials. J Mech Phys Solids 2018;118:115–32. https://doi.org/10.1016/j.jmps.2018.05.012.

[14] Chen T, Bilal OR, Lang R, Daraio C, Shea K. Autonomous deployment of a solar panel using elastic origami and distributed shape-memory-polymer actuators. Phys Rev Appl 2019;11:064069. https://doi.org/10.1103/PhysRevApplied.11.064069.

[15] Morgan J, Magleby SP, Howell LL. An approach to designing origami-adapted aerospace mechanisms. J Mech Des 2016;138:052301. https://doi.org/10.1115/1.4032973.

[16] Bhovad P, Kaufmann J, Li S. Peristaltic locomotion without digital controllers: exploiting multi-stability in origami to coordinate robotic motion. Extrem Mech Lett 2019;32:100552. https://doi.org/10.1016/j.eml.2019.100552.

[17] Felton S, Tolley M, Demaine E, Rus D, Wood R. A method for building self-folding machines. Science 2014;345:644–6. https://doi.org/10.1126/science.1252610.

[18] Dang X, Lu L, Duan H, Wang J. Deployment kinematics of axisymmetric Miura origami: unit cells, tessellations, and stacked metamaterials. Int J Mech Sci 2022;232:107615. https://doi.org/10.1016/j.ijmecsci.2022.107615.

[19] Filipov ET, Tachi T, Paulino GH. Origami tubes assembled into stiff, yet reconfigurable structures and metamaterials. Proc Natl Acad Sci 2015;112:12321–6. https://doi.org/10.1073/pnas.1509465112.

[20] Li Z, Yang Q, Fang R, Chen W, Hao H. Origami metamaterial with two-stage programmable compressive strength under quasi-static loading. Int J Mech Sci 2021;189:105987. https://doi.org/10.1016/j.ijmecsci.2020.105987.

[21] Liu B, Silverberg JL, Evans AA, Santangelo CD, Lang RJ, Hull TC, et al. Topological kinematics of origami metamaterials. Nat Phys 2018;14:811–5. https://doi.org/10.1038/s41567-018-0150-8.

[22] Xiang X, Qiang W, Hou B, Tran P, Lu G. Quasi-static and dynamic mechanical properties of Miura-ori metamaterials. Thin Walled Struct 2020;157:106993. https://doi.org/10.1016/j.tws.2020.106993.

[23] Gillman AS, Fuchi K, Buskohl PR. Discovering sequenced origami folding through nonlinear mechanics and topology optimization. J Mech Des 2019;141:041401. https://doi.org/10.1115/1.4041782.

[24] Hawkes E, An B, Benbernou NM, Tanaka H, Kim S, Demaine ED, et al. Programmable matter by folding. Proc Natl Acad Sci 2010;107:12441–5. https://doi.org/10.1073/pnas.0914069107.

[25] Zhang Q, Wommer J, O’Rourke C, Teitelman J, Tang Y, Robison J, et al. Origami and kirigami inspired self-folding for programming three-dimensional shape shifting of polymer sheets with light. Extrem Mech Lett 2017;11:111–20. https://doi.org/10.1016/j.eml.2016.08.004.

[26] Schenk M, Guest SD. Geometry of Miura-folded metamaterials. Proc Natl Acad Sci 2013;110:3276–81. https://doi.org/10.1073/pnas.1217998110.

[27] Gattas JM, Wu W, You Z. Miura-base rigid origami: parameterizations of first-level derivative and piecewise geometries. J Mech Des 2013;135:111011. https://doi.org/10.1115/1.4025380.

[28] Dudte LH, Vouga E, Tachi T, Mahadevan L. Programming curvature using origami tessellations. Nat Mater 2016;15:583–8. https://doi.org/10.1038/nmat4540.

[29] Yang F, Zhang M, Ma J, You Z, Yu Y, Chen Y, et al. Design of single degree-of-freedom triangular Resch patterns with thick-panel origami. Mech Mach Theory 2022;169:104650. https://doi.org/10.1016/j.mechmachtheory.2021.104650.

[30] Zhou X, Wang H, You Z. Design of three-dimensional origami structures based on a vertex approach. Proc R Soc Math Phys Eng Sci 2015;471:20150407. https://doi.org/10.1098/rspa.2015.0407.

[31] Resch RD, Christiansen H. The design and analysis of kinematic folded-plate systems. In: Proceedings of the IASS Symposium Folded Plates Prismatic Structures; 1970.

[32] Konaković M, Crane K, Deng BS, Piker D, Pauly M. Beyond developable: computational design and fabrication with auxetic materials. ACM Trans Gr 2016;35.

[33] Tachi T, Miura K, Kawasaki T, Tachi T, Uehara R, Lang R, Wang-Iverson P. Rigid folding of periodic origami tessellations. Origami^6. Providence, Rhode Island: American Mathematical Society; 2015. p. 97–108. https://doi.org/10.1090/mbk/095.1/10.

[34] Nassar H, Lebée A, Monasse L. Curvature, metric and parametrization of origami tessellations: theory and application to the eggbox pattern. Proc R Soc Math Phys Eng Sci 2017;473:20160705. https://doi.org/10.1098/rspa.2016.0705.

[35] Kwok TH, Wang CCL, Deng D, Zhang Y, Chen Y. Four-dimensional printing for freeform surfaces: design optimization of origami and kirigami structures. J Mech Des 2015;137:111413. https://doi.org/10.1115/1.4031023.

[36] Oudghiri-Idrissi O, Guzina BB. Effective linear wave motion in periodic origami structures. Comput Methods Appl Mech Eng 2022;399:115386. https://doi.org/10.1016/j.cma.2022.115386.

[37] Woodruff SR, Filipov ET. A bar and hinge model formulation for structural analysis of curved-crease origami. Int J Solids Struct 2020;204–205:114–27. https://doi.org/10.1016/j.ijsolstr.2020.08.010.

[38] Wei ZY, Guo ZV, Dudte L, Liang HY, Mahadevan L. Geometric mechanics of periodic pleated origami. Phys Rev Lett 2013;110:215501. https://doi.org/10.1103/PhysRevLett.110.215501.

[39] Fuchi K, Buskohl PR, Bazzan G, Durstock MF, Reich GW, Vaia RA, et al. Origami actuator design and networking through crease topology optimization. J Mech Des 2015;137:091401. https://doi.org/10.1115/1.4030876.

[40] Rodrigues GV, Savi MA. Reduced-order model description of origami stent built with waterbomb pattern. Int J Appl Mech 2021;13:2150016. https://doi.org/10.1142/S1758825121500162.

[41] Barbieri E, Ventura L, Bilotti E. Numerical simulations of folding mechanics in nonlinear plates using discontinuous rotations. Int J Solids Struct 2022;249:111675. https://doi.org/10.1016/j.ijsolstr.2022.111675.

[42] Liu K, Paulino GH. Nonlinear mechanics of non-rigid origami: an efficient computational approach. Proc R Soc Math Phys Eng Sci 2017;473:20170348. https://doi.org/10.1098/rspa.2017.0348.

[43] Liu K, Novelino LS, Gardoni P, Paulino GH. Big influence of small random imperfections in origami-based metamaterials. Proc R Soc Math Phys Eng Sci 2020;476:20200236. https://doi.org/10.1098/rspa.2020.0236.

[44] Chen Y, Fan L, Bai Y, Feng J, Sareh P. Assigning mountain-valley fold lines of flat-foldable origami patterns based on graph theory and mixed-integer linear programming. Comput Struct 2020;239:106328. https://doi.org/10.1016/j.compstruc.2020.106328.

[45] Huang K, Song K, Zhou X, Ji B, Wang H. Quasi-static mechanical properties of composite foldcores based on the BCH patterns. Thin Walled Struct 2022;171:108776. https://doi.org/10.1016/j.tws.2021.108776.

[46] Kumar P, Pellegrino S. Computation of kinematic paths and bifurcation points. Int J Solids Struct 2000;37:7003–27. https://doi.org/10.1016/S0020-7683(99)00327-3.

[47] Stern M, Pinson MB, Murugan A. The complexity of folding self-folding origami. Phys Rev X 2017;7:041070. https://doi.org/10.1103/PhysRevX.7.041070.

[48] Fang H, Li S, Ji H, Wang KW. Dynamics of a bistable Miura-origami structure. Phys Rev E 2017;95:052211. https://doi.org/10.1103/PhysRevE.95.052211.

[49] Sadeghi S, Li S. Dynamic folding of origami by exploiting asymmetric Bi-stability. Extrem Mech Lett 2020;40:100958. https://doi.org/10.1016/j.eml.2020.100958.

[50] Wu H, Fang H, Chen L, Xu J. Transient dynamics of a miura-origami tube during free deployment. Phys Rev Appl 2020;14:034068. https://doi.org/10.1103/PhysRevApplied.14.034068.

[51] Yu Y, Paulino GH, Luo Y. Finite particle method for progressive failure simulation of truss structures. J Struct Eng 2011;137:1168–81. https://doi.org/10.1061/(ASCE)ST.1943-541X.0000321.

[52] Yu Y, Zhao X, Luo Y. Multi-snap-through and dynamic fracture based on finite particle method. J Constr Steel Res 2013;82:142–52. https://doi.org/10.1016/j.jcsr.2012.12.019.

[53] Yu Y, Chen Y, Paulino GH. On the Unfolding process of triangular resch patterns: a finite particle method investigation. Vol. 5B. In: Proceedings of the 43rd Mechnical Robotics Conference. Anaheim, California, USA: American Society of Mechanical Engineers; 2019. https://doi.org/10.1115/DETC2019-98121. V05BT07A048.

[54] Deng A, Ji B, Zhou X, You Z. Geometric design and mechanical properties of foldcores based on the generalized Resch patterns. Thin Walled Struct 2020;148:106516. https://doi.org/10.1016/j.tws.2019.106516.

[55] Liang H, Hao G, Olszewski OZ, Jiang Z, Zhang K. Design of a foldable origami mechanism with helical motion inspired by the Resch triangular tessellation. Mech Mach Theory 2023;179:105101. https://doi.org/10.1016/j.mechmachtheory.2022.105101.

[56] Ma J, Zang S, Chen Y, You Z. The tessellation rule and properties programming of origami metasheets built with a mixture of rigid and non-rigid square-twist patterns. Engineering 2022. https://doi.org/10.1016/j.eng.2022.02.015.

[57] Magliozzi L, Micheletti A, Pizzigoni A, Ruscica G. On the design of origami structures with a continuum of equilibrium shapes. Compos Part B Eng 2017;115: 144–50. https://doi.org/10.1016/j.compositesb.2016.10.023.

[58] Yu Y, Zhu X. Nonlinear dynamic collapse analysis of semi-rigid steel frames based on the finite particle method. Eng Struct 2016;118:383–93. https://doi.org/10.1016/j.engstruct.2016.03.063.

[59] Dong S, Zhao X, Yu Y. Dynamic unfolding process of origami tessellations. Int J Solids Struct 2021;226–227:111075. https://doi.org/10.1016/j.ijsolstr.2021.111075.

[60] Dong S, Yu Y. Numerical and experimental studies on capturing behaviors of the inflatable manipulator inspired by fluidic origami structures. Eng Struct 2021;245: 112840. https://doi.org/10.1016/j.engstruct.2021.112840.

[61] Xue Y, Luo Y, Xu X, Wan HP, Shen Y. A robust method for pre-stress adjustment of cable-strut structures based on sparse regression. Eng Struct 2021;246:112987. https://doi.org/10.1016/j.engstruct.2021.112987.

[62] Samy A, Yuan X, Zhang Y, Zhang W. Study on bagging effect and rupture failure of membrane structures. Eng Struct 2021;232:111880. https://doi.org/10.1016/j.engstruct.2021.111880.

[63] Han SE, Lee KS. A study of the stabilizing process of unstable structures by dynamic relaxation method. Comput Struct 2003;81:1677–88. https://doi.org/10.1016/S0045-7949(03)00187-1.

[64] Pauletti RMO, Rocha KB. A simple finite element framework for modelling pneumatic structures. Eng Struct 2021;235:111812. https://doi.org/10.1016/j.engstruct.2020.111812.

[65] Jahromi HZ, Izzuddin BA. Energy conserving algorithms for dynamic contact analysis using Newmark methods. Comput Struct 2013;118:74–89. https://doi.org/10.1016/j.compstruc.2012.07.012.

[66] Kokusho T, Mori J, Mizuhara M, Fang H. Energy-based Newmark method for seismic slope displacements revisited. Soil Dyn Earthq Eng 2022;162:107449. https://doi.org/10.1016/j.soildyn.2022.107449.

[67] Krenk S. Energy conservation in Newmark based time integration algorithms. Comput Methods Appl Mech Eng 2006;195:6110–24. https://doi.org/10.1016/j.cma.2005.12.001.

[68] Tachi T. Designing freeform origami tessellations by generalizing Resch's patterns. J Mech Des 2013;135:111006. https://doi.org/10.1115/1.4025389.

[69] Ritto-Corrêa M, Camotim D. On the differentiation of the Rodrigues formula and its significance for the vector-like parameterization of Reissner-Simo beam theory: differentiation of rodrigues formula. Int J Numer Methods Eng 2002;55:1005–32. https://doi.org/10.1002/nme.532.

[70] Van Schaik R, Berendsen H, Torda A, Van Gunsteren W. A structure refinement method based on molecular dynamics in four spatial dimensions. J Mol Biol 1993; 234:751–62.

[71] Dharmadasa BY, Mallikarachchi HMYC, Lopez Jimenez F. Characterizing the mechanics of fold-lines in thin Kapton membranes. In: Proceedings of the AIAA Spacecraft Structures Conference. Kissimmee, Florida: American Institute of Aeronautics and Astronautics; 2018. https://doi.org/10.2514/6.2018-0450.